CHAPTER 4

Robust Finite Difference Scheme for Non-linear Generalized Time-Fractional Diffusion Equation with Non-smooth Solution

This chapter aims to develop a stable multi-step numerical scheme for the non-linear generalized time-fractional diffusion equations (GTFDEs) with non-smooth solutions. Mesh grading technique is used to discretize the temporal direction which results in $2-\alpha$ order of convergence ($0 < \alpha < 1$). Sect. 4.1 gives a brief description about the non-linear mathematical model proposed in this chapter and few basic definitions. Sect. 4.2 presents the multi-step difference scheme for the non-linear model problem where the non-linear source term is approximated using Taylor's series. Theoretical stability and convergence analysis is established in the L_2-norm in Sect. 4.3. Some random noise perturbations are added to investigate the numerical stability of the developed scheme in Sect. 4.4. Also, numerical simulations are

performed on three test examples to verify the robustness and efficiency of the scheme. Sect. 4.5 concludes the chapter.

4.1 Introduction

In a rectangle $H(x,t) = [0,1] \times [0,T]$ consider the following GTFDE with variable coefficients satisfying the Dirichlet boundary conditions.

$$\partial_{0,t}^{\alpha,\omega(t)}\zeta(x,t) = \mathcal{L}\zeta(x,t) + G(x,t) + f(\zeta), \quad x \in (0,1), \quad 0 < t \leq T, \tag{4.1a}$$

$$\zeta(0,t) = 0, \quad \zeta(1,t) = 0, \quad 0 \leq t \leq T, \quad \zeta(x,0) = \zeta_0(x), \quad x \in [0,1], \tag{4.1b}$$

where,

$$\partial_{0,t}^{\alpha,\omega(t)}\zeta(x,t) = \frac{1}{\Gamma(1-\alpha)} \int_0^t \frac{\omega(t-\xi)}{(t-\xi)^{\alpha}} \frac{\partial \zeta(x,\xi)}{\partial \xi} d\xi, \quad \alpha \in (0,1), \tag{4.2}$$

is the Caputo FD with generalized memory kernel characterized by the weight function $\omega(t) \in C^2[0,T]$ such that $\omega(t) > 0$, $\omega'(t) \leq 0$. The operator $\mathcal{L}$ in equation (4.1a) has the following definition

$$\mathcal{L}\zeta(x,t) = \frac{\partial}{\partial x}\left(m(x,t)\frac{\partial \zeta}{\partial x}\right) - p(x,t)\zeta, \tag{4.3}$$

in which $m(x,t) \geq c_1 > 0$ and $p(x,t) \geq 0$ are the given functions. $G(x,t)$ is the linear source term and $f(\zeta)$ is the non-linear reaction term satisfying the following

assumed conditions [103].

$$F_1 : |f(\zeta)| \leq C|\zeta|, \qquad F_2 : \ |f'(\zeta)| \leq C.$$

It is noteworthy that the solution $\zeta(x,t)$ of (4.1) is non-smooth and its derivative has a singular nature at the starting point $t = 0$ and satisfies the following weak regularity conditions [55].

$$\left|\frac{\partial^k \zeta(x,t)}{\partial t^k}\right| \leq C(1+t^{\alpha-k}) \text{ for } 0 \leq k \leq 2, \tag{4.4a}$$

$$\left|\frac{\partial^l \zeta(x,t)}{\partial x^l}\right| \leq C \ \text{ for } 0 \leq l \leq 2, \tag{4.4b}$$

for all $(x,t) \in [0,1] \times (0,T]$.

The motivation behind considering the non-linear model (4.1) of GTFDEs is that most systems are intrinsically non-linear in nature. The non-linear forced term is basically a reaction term added to the diffusion equation that increases the energy of the system and may cause the solution to blow up in a finite time. Therefore, many available research articles focused on different non-linear models of fractional calculus. Adding to the non-linear complexity of the model (4.1) it is also clear from equation (4.4) that the temporal derivatives of the solution $\zeta(x,t)$ of these models blow up as $t \to 0$. This typical singularity of the solution creates difficulty in finding the numerical solution to the mathematical model (4.1). Many authors [104–106] used uniform discretization for TFDEs with smooth solutions but a uniform grid yields poor results for the non-smooth solutions. Consequently, mesh refinement techniques [54, 55, 59, 107] has developed as one of the significant tools to handle the singularity of such non-smooth solutions.

In the currently available literature, numerical techniques have been designed only for the linear GTFDEs models till date. Therefore, the purpose of this article is to design stable and robust numerical scheme for finding the numerical solution to the non-linear GTFDE model (4.1). The contribution of this chapter can be summarized through the below listed points.

- Stable multistep scheme has been designed for the non-linear initial-boundary value problem (4.1) . The non-linear reaction term satisfying the conditions F_1 and F_2 has been linearized using Taylor's series approximation.
- Graded mesh technique has been utilized in the L1 formula for GTFDEs to tackle the singularity of non-smooth solution at the initial point $t = 0$. Using this grid refinement method the developed scheme has much higher CO as compared to the uniform temporal discretization.
- Theoretical stability and convergence analysis of the scheme has been investigated in the L_2-norm for the non-smooth solutions. Thus, the difference scheme is proved to have a convergence order of $O(N^{\alpha-2} + h^2)$.
- To test the robustness and efficiency of the scheme three test problems have been experimented using the developed scheme. The results obtained are compared on both uniform and non-uniform grid. The non-uniform temporal mesh grading produces much better results than the uniform case.
- Finally, numerical analysis has been investigated by introducing some noise perturbations to the given initial condition, both linear and non-linear source terms.

Notation: Throughout the chapter $C \in \mathbb{R}^+$ is a constant independent of both the temporal and spatial discretization parameters and can have different values at different places.

4.2 Difference scheme and generalized fractional derivative's approximation

Firstly, we present the L1 formula for the generalized Caputo FD on a general mesh [69]. Then we design the difference scheme considering the above non-uniform L1 formula.

4.2.1 L1 approximation

For $N \in \mathbb{Z}^+$, consider the general temporal mesh $\chi_\tau = \{0 = t_0 < t_1 < t_2 \ldots < t_N = T\}$ with the time step size τ_{n+1} defined by $\tau_{n+1} = t_{n+1} - t_n$, for $0 \leq n \leq N-1$. Then for any mesh dependent function $\zeta(t) \in C[0,T] \cap C^2(0,T]$, we approximate the generalized derivative $\partial^{\alpha,\omega(t)}_{0,t_{n+1}}\zeta(t)$ of order α, $\alpha \in (0,1)$, with a weight function $\omega(t) \in C^2[0,T]$ using the linear interpolation of $\zeta(t)$. So we have

$$\begin{aligned}\partial^{\alpha,\omega(t)}_{0,t_{n+1}}\zeta(t) &= \frac{1}{\Gamma(1-\alpha)}\int_0^{t_{n+1}} \frac{\omega(t_{n+1}-\nu)\zeta'(\nu)}{(t_{n+1}-\nu)^\alpha}d\nu = \frac{1}{\Gamma(1-\alpha)}\sum_{s=0}^{n}\int_{t_s}^{t_{s+1}} \frac{\omega(t_{n+1}-\nu)\zeta'(\nu)}{(t_{n+1}-\nu)^\alpha}d\nu \\ &= \frac{1}{\Gamma(1-\alpha)}\sum_{s=0}^{n}\zeta_{t,s}\int_{t_s}^{t_{s+1}} \frac{\omega(t_{n+1}-\nu)}{(t_{n+1}-\nu)^\alpha}d\nu + R_1,\end{aligned}$$

where

$$\zeta_{t,s} = \frac{\zeta(t_{s+1}) - \zeta(t_s)}{\tau_{s+1}}, \quad R_1 = \frac{1}{\Gamma(1-\alpha)} \sum_{s=0}^{n} \int_{t_s}^{t_{s+1}} \frac{(\zeta(\nu) - \Pi_{1,s}\zeta(\nu))'\omega(t_{n+1} - \nu)}{(t_{n+1} - \nu)^{\alpha}} d\nu,$$

For the weighting function $\omega(t_{n+1} - \nu)$, using second order approximation in the interval $[0, t_{n+1}]$ we get,

$$\omega(t_{n+1} - \nu) = \omega(t_{n+1} - t_s - \frac{\tau_{s+1}}{2}) + (\omega(t_{n+1} - t_{s+1}) - \omega(t_{n+1} - t_s))(\nu - 1/2) + O(\tau^2)$$

Set $\Psi(\nu) = \omega(t_{n+1} - t_s - \frac{\tau_{s+1}}{2}) + (\omega(t_{n+1} - t_{s+1}) - \omega(t_{n+1} - t_s))(\nu - \frac{1}{2})$, hence

$$\begin{aligned}
\partial_{0,t_{n+1}}^{\alpha,\omega(t)} \zeta(t) &= \frac{1}{\Gamma(1-\alpha)} \sum_{s=0}^{n} \zeta_{t,s} \int_{t_s}^{t_{s+1}} \frac{\Psi(\nu)}{(t_{n+1} - \nu)^{\alpha}} d\nu + R_1 + R_2 \\
&= \frac{1}{\Gamma(2-\alpha)} \sum_{s=0}^{n} \Big[\omega(t_{n+1} - t_s - \frac{\tau_{s+1}}{2}) a_s^{n+1} + (\omega(t_{n+1} - t_{s+1}) \\
&\quad - \omega(t_{n+1} - t_s)) b_s^{n+1} \Big] (\zeta_{s+1} - \zeta_s) + R_1 + R_2,
\end{aligned}$$

where,

$$\begin{aligned}
a_s^{n+1} &= \frac{(t_{n+1} - t_s)^{1-\alpha} - (t_{n+1} - t_{s+1})^{1-\alpha}}{\tau_{s+1}}, \\
b_s^{n+1} &= \frac{1}{\tau_{s+1}^2} \Bigg(\frac{1}{2-\alpha} [(t_{n+1} - t_s)^{2-\alpha} - (t_{n+1} - t_{s+1})^{2-\alpha}] - \\
&\quad \frac{\tau_{s+1}}{2} [(t_{n+1} - t_s)^{1-\alpha} + (t_{n+1} - t_{s+1})^{1-\alpha}] \Bigg), \\
R_2 &= \frac{1}{\Gamma(1-\alpha)} \sum_{s=0}^{n} \int_{t_s}^{t_{s+1}} \frac{\zeta_{t,s}(\omega(t_{n+1} - \nu) - \Psi(\nu))}{(t_{n+1} - \nu)^{\alpha}} d\nu,
\end{aligned}$$

Hence, the L1 formula for generalized Caputo FD of order α with weight $\omega(t)$ $(\alpha \in (0,1),\ \omega(t) > 0,\ \omega'(t) \leq 0)$ on a general mesh is:

$$\Delta_{0,t_{n+1}}^{\alpha,\omega(t)}\zeta = \sum_{s=0}^{n} c_s^{n+1}(\zeta(t_{s+1}) - \zeta(t_s)), \tag{4.5}$$

$$c_s^{n+1} = \frac{1}{\Gamma(2-\alpha)}\left[\omega(t_{n+1} - t_s - \frac{\tau_{s+1}}{2})a_s^{n+1} + (\omega(t_{n+1} - t_{s+1}) - \omega(t_{n+1} - t_s))b_s^{n+1}\right].$$

4.2.2 Multi-step scheme for the non-linear GTFDEs

Let $\zeta(x,t) \in H$ with $\zeta(t) \in C[0,T] \cap C^2(0,T]$, $\zeta(x) \in C^4[0,L]$, be the exact solution of the problem (4.1) satisfying the weak regularity conditions (4.4).

To obtain a finite difference multi-step scheme, we approximate the non-linear reaction term using Taylor's series expansion of $f(\zeta^{n+1})$. For the first time-level t_{n+1} at $n = 0$, we use linear approximation (because ζ^n is known for $n = 0$),

$$f(\zeta^{n+1}) = f(\zeta^n) + O(\tau), \tag{4.6a}$$

and for $n \geq 1$, we use a second order approximation

$$f(\zeta^{n+1}) = 2f(\zeta^n) - f(\zeta^{n-1}) + O(\tau^2). \tag{4.6b}$$

4.2.2.1 Scheme

Here we derive a multi-step scheme for the non-linear GTFDEs (4.1). Let $M \in \mathbb{Z}^+$ and the uniform space step size $h = l/M$. Then $\chi_h = \{x_i = ih,\ i = 0,1,2,\ldots,M-1\}$ and $\chi_\tau = \{0 = t_0 < t_1 < t_2 \ldots < t_N = T\}$. In the rectangle $H = \chi_h \times \chi_\tau = [0,1] \times [0,T]$, let $\varpi(x,t)$ be the numerical solution to the model (4.1). Using (4.5)

and (4.6), we assign the following multi-step difference scheme to the problem (4.1).

Case1: For $n = 0$,

$$\Delta_{0,t_{n+1}}^{\alpha,\omega(t)}\varpi_i = \wedge\varpi_i^{n+1} + G_i^{n+1} + f(\varpi^n), \quad i = 1, 2, \ldots, M-1, \tag{4.7a}$$

Case2: For $1 \leq n \leq N-1$,

$$\Delta_{0,t_{n+1}}^{\alpha,\omega(t)}\varpi_i = \wedge\varpi_i^{n+1} + G_i^{n+1} + 2f(\varpi^n) - f(\varpi^{n-1}), \quad 1 \leq i \leq M-1, \tag{4.7b}$$

$$\varpi(0,t) = 0,\ \varpi(l,t) = 0,\ t \in \chi_\tau,\ \varpi(x,0) = \zeta_0(x),\ x \in \chi_h, \tag{4.8}$$

where,

$$(\wedge\varpi)_i = ((a\varpi_{\bar{x}})_x - d\varpi)_i = \frac{a_{i+1}\varpi_{i+1} - (a_{i+1}+a_i)\varpi_i + a_i\varpi_{i-1}}{h^2} - d_i\varpi_i,\ \ 1 \leq i \leq M-1,$$

$$\varpi_{\bar{x},i} = \frac{\varpi_i - \varpi_{i-1}}{h},\ \varpi_{x,i} = \frac{\varpi_{i+1} - \varpi_i}{h},\ \ a_i^{n+1} = m(x_{i-1/2}, t_{n+1}),$$
$$d_i^{n+1} = p(x_i, t_{n+1}),\ \ G_i^{n+1} = G(x_i, t_{n+1}).$$

From Lemma 3.1 in [47]

$$\mathcal{L}\zeta|_{(x_i,t_{n+1})} = \wedge\zeta(x_i, t_{n+1}) + O(h^2),\ \ 1 \leq i \leq M-1. \tag{4.9}$$

Mesh grading: The formula for the non-uniform mesh grading can be stated as the following [55]

$$t_n = T(n/N)^r \quad \text{for} \quad n = 0, 1, 2, \ldots, N, \tag{4.10}$$

where the constant mesh grading $r \geq 1$ is a user chosen number. It can be easily shown that

$$\tau_{n+1} = t_{n+1} - t_n \leq CTN^{-r}n^{r-1} \quad \text{for } n = 1, 2, \ldots, N-1, \tag{4.11}$$

4.3 Theoretical analysis

Lemma 4.3.1. [69] For any $0 \leq n \leq N-1$ $\{a_s^{n+1} \ |0 \leq s \leq n\}$, $\alpha \in (0,1)$ and $\omega(t) \in C^2[0,T]$ the subsequent inequality holds :

$$a_n^{n+1} > a_{n-1}^{n+1} > \ldots > a_s^{n+1} > a_{s-1}^{n+1} > \ldots a_0^{n+1} > \frac{1-\alpha}{t_{n+1}^{\alpha}},$$

$$b_n^{n+1} > b_{n-1}^{n+1} > \ldots > b_s^{n+1} > b_{s-1}^{n+1} > \ldots > b_0^{n+1} > 0,$$

$$c_n^{n+1} > c_{n-1}^{n+1} > \ldots > c_s^{n+1} > c_{s-1}^{n+1} > \ldots c_0^{n+1} > \frac{\omega(t_{n+1} - 0.5\tau_1)}{\Gamma(1-\alpha)t_{n+1}^{\alpha}}.$$

Proof. The proof for this Lemma can be found in the work [69]. □

Lemma 4.3.2. [108] Let ${}^{C}D_t^{\alpha}\zeta(t) = \sum_{j=0}^{n} K_{n-j}^{n+1}(\zeta(t_{j+1}) - \zeta(t_j))$ be the approximation of the classical Caputo derivative

$${}^{C}D_t^{\alpha}\zeta(t) = \frac{1}{\Gamma(1-\alpha)}\int_0^t \frac{\zeta'(\xi)}{(t-\xi)^{\alpha}}d\xi, \quad \alpha \in (0,1),$$

with

$$K_0^{n+1} \geq K_1^{n+1} \geq \ldots \geq K_n^{n+1}, \quad 0 \leq n \leq N-1, \tag{4.12a}$$

and there exist a constant π_K such that

$$K_{n-j}^{n+1} \geq \frac{1}{\Gamma(1-\alpha)\pi_K \tau_{j+1}} \int_{t_j}^{t_{j+1}} (t_{n+1}-s)^{-\alpha} ds, \ 0 \leq j \leq n \leq N-1, \tag{4.12b}$$

and $(G^{n+1})_{n=0}^{N-1}$ and $(\lambda_n)_{n=0}^{N-1}$ be given non-negative sequences. Moreover, assume there exist a constant Λ independent of the step sizes such that $\Lambda \geq \sum_{n=0}^{N-1} \lambda_n$ and

$$\max_{0\leq n\leq N-1} \tau_{n+1} \leq \frac{1}{\sqrt[\alpha]{2\Lambda\pi_K\Gamma(2-\alpha)}},$$

Then for any non-negative sequence $(\zeta^j)_{j=0}^{N}$ satisfying

$$\sum_{j=0}^{n} K_{n-j}^{n+1}((\zeta^{j+1})^2 - (\zeta^j)^2) \leq \sum_{j=1}^{n+1} \lambda_{n+1-j}(\zeta^j)^2 + \zeta^{n+1}G^{n+1}, \text{ for } 0 \leq n \leq N-1, \tag{4.13}$$

By Discrete fractional Gronwall inequality the following holds

$$\zeta^{n+1} \leq 2E_{\alpha}(2max(1,\rho)\pi_K \Lambda t_{n+1}^{\alpha}) \left(\zeta^0 + \max_{0\leq j\leq n} \sum_{k=1}^{j+1} \Theta_{j+1-k}^{j+1} G^k\right), \ \forall\ 0 \leq n \leq N-1, \tag{4.14}$$

where E_α denote the Mittag-Lefter function,

$$E_\alpha(y) = \sum_{k=0}^{\infty} \frac{y^k}{\Gamma(1+k\alpha)},$$

Θ^{n+1} are discrete functions satisfying the following reccurence relation

$$\Theta_0^{n+1} = \frac{1}{K_0^{n+1}}, \quad \Theta_k^{n+1} = \frac{1}{K_0^{n+1-k}} \sum_{j=0}^{k-1} (K_{k-j-1}^{n+1-j} - K_{k-j}^{n+1-j})\Theta_j^{n+1}, \quad 1 \le k \le n,$$

and $\rho > 0$ is a constant such that the step size ratios $\rho_n = \tau_n/\tau_{n+1}$ satisfy the condition $\rho_n \le \rho$, $\forall\ 1 \le n \le N-1$.

Proof. See [108] for more details. □

Theorem 4.3.1. The numerical solution ϖ_i^n $\{0 \le i \le M,\ n = 0, 1, \dots N\}$ to the problem (4.1) satisfies the below inequality and hence the numerical scheme (4.7) is unconditionally stable.

$$||\varpi^{n+1}||_0^2 \le 2E_\alpha\left(24C\max(1,\rho)\frac{t_{n+1}^\alpha}{\omega(T)}\right)\left(||\varpi^0||_0^2 + \underset{0\le j\le n}{max}\sum_{k=1}^{j+1}\Theta_{j+1-k}^{j+1}||G^k||_0^2\right),\ \forall\, 0 \le n \le N-1. \tag{4.15}$$

Proof. The inner product of equation (4.7b) with ϖ^{n+1} yields

$$(\Delta_{0,t_{n+1}}^{\alpha,\omega(t)}\varpi, \varpi^{n+1}) - (\wedge\varpi^{n+1}, \varpi^{n+1}) = (G^{n+1}, \varpi^{n+1}) + (2f(\varpi^n) - f(\varpi^{n-1}), \varpi^{n+1}).$$

Using the positive definite property of the operator $\wedge = -\wedge$ and applying Green's Formula from $x = 0$ to l, we get $(-\wedge\varpi^{n+1}, \varpi^{n+1}) \ge \varkappa||\varpi^{n+1}||_0^2$, $\varkappa > 0$, hence dropping this positive term, we get

$$(\Delta_{0,t_{n+1}}^{\alpha,\omega(t)}\varpi, \varpi^{n+1}) \le (G^{n+1}, \varpi^{n+1}) + (2f(\varpi^n) - f(\varpi^{n-1}), \varpi^{n+1}), \tag{4.16}$$

Simplifying further we get,

$$(\Delta_{0,t_{n+1}}^{\alpha,\omega(t)}\varpi) = \sum_{s=0}^{n} c_s^{n+1}(\varpi^{s+1} - \varpi^s)$$
$$= \sum_{s=0}^{n} c_{n-s}^{n+1}(\varpi^{n-s+1} - \varpi^{n-s}) = \sum_{s=0}^{n} d_s^{n+1}(\varpi^{n-s+1} - \varpi^{n-s}) = \sum_{s=0}^{n} d_{n-s}^{n+1}(\varpi^{s+1} - \varpi^s),$$

where $d_s^{n+1} = c_{n-s}^{n+1}$ and $d_{s+1}^{n+1} = c_{n-s-1}^{n+1}$. Also, since the following inequality is true for any mesh function $z(t)$ defined on the grid χ_τ,

$$z^n \Delta_{0,t_n}^{\alpha,\omega(t)} z \geq \frac{1}{2}\Delta_{0,t_n}^{\alpha,\omega(t)}(z^2),\ n = 1, 2, \ldots, N \quad \text{(see [45])}.$$

Thus

$$(\Delta_{0,t_{n+1}}^{\alpha,\omega(t)}\varpi, \varpi^{n+1}) \geq \frac{1}{2}\Delta_{0,t_{n+1}}^{\alpha,\omega(t)}\varpi^2 = \frac{1}{2}\sum_{s=0}^{n} d_{n-s}^{n+1}((\varpi^{s+1})^2 - (\varpi^s)^2), \tag{4.17}$$

Hence, using (4.17) in (4.16) yields

$$\frac{1}{2}\sum_{s=0}^{n} d_{n-s}^{n+1}((\varpi^{s+1})^2 - (\varpi^s)^2) \leq (G^{n+1}, \varpi^{n+1}) + (2f(\varpi^n) - f(\varpi^{n-1}), \varpi^{n+1}),$$

Noting the condition F_1 to be true and using Cauchy Schwarz inequality gives

$$\sum_{s=0}^{n} d_{n-s}^{n+1}((\varpi^{s+1})^2 - (\varpi^s)^2) \leq 4C(||\varpi^{n-1}||_0^2 + ||\varpi^n||_0^2 + ||\varpi^{n+1}||_0^2)$$
$$+ (G^{n+1}, \varpi^{n+1}),\ 1 \leq n \leq N-1. \tag{4.18}$$

For $n = 0$ case, multiplying (4.7a) by ϖ^1 and following similar steps to $n \geq 1$ case, we get

$$d_0^1((\varpi^1)^2 - (\varpi^0)^2) \leq 4(||\varpi^0||_0^2 + ||\varpi^1||_0^2) + (G^1, \varpi^1),$$

Also from Lemma (4.3.1), it is clear that

$$d_0^{n+1} > d_1^{n+1} > \ldots > d_n^{n+1} > 0, \tag{4.19}$$

and

$$\begin{aligned} c_s^{n+1} =& \frac{1}{\Gamma(2-\alpha)} \left[\omega(t_{n+1} - t_s - \frac{\tau_{s+1}}{2})a_s^{n+1} + (\omega(t_{n+1} - t_{s+1}) - \omega(t_{n+1} - t_s))b_s^{n+1}\right], \\ >& \frac{1}{\Gamma(2-\alpha)}\omega(t_{n+1} - t_s - \frac{\tau_{s+1}}{2})a_s^{n+1} \\ >& \frac{\omega(T)}{\Gamma(2-\alpha)}a_s^{n+1}, \quad (\text{since } \omega(T) \text{ is decreasing and } b_s^{n+1} > 0), \end{aligned}$$

Thus,

$$d_s^{n+1} > \frac{\omega(T)}{\Gamma(2-\alpha)}a_s^{n+1}. \tag{4.20}$$

Now, using $K_{n-s}^{n+1} = d_{n-s}^{n+1}$ and since the conditions (4.19)-(4.20) are similar to equations (4.12a)-(4.12b). Hence, applying the Discrete fractional Gronwall inequality defined in Lemma (4.3.2) with $\pi_K = 1/\omega(t)$, $\Lambda = 12C$ in equation (4.18) yields the required a priori estimate (4.15). □

Lemma 4.3.3. Let $\zeta \in C[0,T] \cap C^2(0,T]$ satisfy the conditions (4.4). Then for any $\alpha \in (0,1)$ and weight function $\omega(t) \in C^2[0,T]$

$$|\partial_{0,t_{n+1}}^{\alpha,\omega(t)}\zeta - \Delta_{0,t_{n+1}}^{\alpha,\omega(t)}\zeta| \leq CN^{-min\{2-\alpha,r\alpha\}}, \text{ for } n = 0,1,\ldots,N-1.$$

Proof. Since,

$$\partial_{0,t_{n+1}}^{\alpha,\omega(t)}\zeta - \Delta_{0,t_{n+1}}^{\alpha,\omega(t)}\zeta = R_1 + R_2$$

where,

$$R_1 = \frac{1}{\Gamma(1-\alpha)} \sum_{s=0}^{n} \int_{t_s}^{t_{s+1}} \frac{(\zeta(\nu) - \Pi_{1,s}\zeta(\nu))'\omega(t_{n+1}-\nu)}{(t_{n+1}-\nu)^{\alpha}} d\nu,$$
$$R_2 = \frac{1}{\Gamma(1-\alpha)} \sum_{s=0}^{n} \int_{t_s}^{t_{s+1}} \frac{\zeta_{t,s}(\omega(t_{n+1}-\nu) - \Psi(\nu))}{(t_{n+1}-\nu)^{\alpha}} d\nu,$$

Since $\omega(t_{n+1}-\nu) \in C^2[0,T]$, denote $n_1 = \sup_{\nu\in[t_s,t_{s+1}]} |\omega'(\nu)|$,

$$\begin{aligned}
R_1 &= \frac{1}{\Gamma(1-\alpha)} \left| \sum_{s=0}^{n} \int_{t_s}^{t_{s+1}} \frac{\omega(t_{n+1}-\nu)(\zeta(\nu) - \Pi_{1,s}\zeta(\nu))'}{(t_{n+1}-\nu)^{\alpha}} d\nu \right| \\
&\leq \frac{1}{\Gamma(1-\alpha)} \left| \sum_{s=1}^{n-1} \int_{t_s}^{t_{s+1}} \frac{\omega(t_{n+1}-\nu)(\zeta(\nu) - \Pi_{1,s}\zeta(\nu))'}{(t_{n+1}-\nu)^{\alpha}} d\nu \right| \\
&+ \frac{1}{\Gamma(1-\alpha)} \int_{t_n}^{t_{n+1}} \frac{\omega(t_{n+1}-\nu)|\zeta'(\nu) - v_{t,n}|}{(t_{n+1}-\nu)^{\alpha}} d\nu \\
&+ \frac{1}{\Gamma(1-\alpha)} \int_{0}^{t_1} \frac{\omega(t_{n+1}-\nu)}{(t_{n+1}-\nu)^{\alpha}} \left| \frac{v_1 - v_0}{\tau_1} - \frac{\partial\zeta}{\partial\nu} \right| d\nu \\
&\leq \frac{1}{\Gamma(1-\alpha)} \left[\sum_{s=1}^{n-1} \int_{t_s}^{t_{s+1}} \frac{|\omega'(t_{n+1}-\nu)||\zeta(\nu) - \Pi_{1,s}\zeta(\nu)|}{(t_{n+1}-\nu)^{\alpha}} d\nu \right. \\
&\left. + \alpha \sum_{s=1}^{n-1} \int_{t_s}^{t_{s+1}} \frac{\omega(t_{n+1}-\nu)|\zeta(\nu) - \Pi_{1,s}\zeta(\nu)|}{(t_{n+1}-\nu)^{\alpha+1}} d\nu \right] \\
&+ \frac{1}{\Gamma(1-\alpha)} \int_{t_n}^{t_{n+1}} \frac{\omega(t_{n+1}-\nu)|\zeta'(\nu) - \zeta_{t,n}|}{(t_{n+1}-\nu)^{\alpha}} d\nu \\
&+ \frac{1}{\Gamma(1-\alpha)} \int_{0}^{t_1} \frac{\omega(t_{n+1}-\nu)}{(t_{n+1}-\nu)^{\alpha}} \left| \frac{\zeta_1 - \zeta_0}{\tau_1} - \frac{\partial\zeta}{\partial\nu} \right| d\nu \\
&\leq Cn_1N^{-2} + C\alpha\omega(0)N^{-(2-\alpha)} + C\omega(0)N^{-(2-\alpha)} + C\omega(0)N^{-r\alpha}, \quad \text{(see Lemma (4.4) [69])}.
\end{aligned}$$

Similarly, denote $n_2 = \sup_{\nu\in[t_s,t_{s+1}]} |\omega''(\nu)|$.

$$R_2 \leq \frac{1}{\Gamma(1-\alpha)} \sum_{s=0}^{n} \int_{t_s}^{t_{s+1}} \frac{|\zeta_{t,s}(\omega(t_{n+1}-\nu) - \Psi(\nu))|}{(t_{n+1}-\nu)^{\alpha}} d\nu$$

$$\leq \frac{n_2}{4\Gamma(1-\alpha)} \sum_{s=0}^{n} \tau_{s+1}^2 \int_{t_s}^{t_{s+1}} \frac{\zeta_{t,s}}{(t_{n+1}-\nu)^{\alpha}} d\nu$$

using condition (4.4) gives

$$\leq \frac{n_2\tau_1}{4\Gamma(1-\alpha)}(\zeta_1-\zeta_0) \int_0^{t_1} (t_{n+1}-\nu)^{-\alpha} d\nu + \frac{Cn_2}{4\Gamma(1-\alpha)} \sum_{s=1}^{n-1} t_s^{\alpha-1}\tau_{s+1}^2$$

$$\int_{t_s}^{t_{s+1}} (t_{n+1}-\nu)^{-\alpha} d\nu + \frac{n_2\tau_{n+1}}{4\Gamma(1-\alpha)}(\zeta_{n+1}-\zeta_n) \int_{t_n}^{t_{n+1}} (t_{n+1}-\nu)^{-\alpha} d\nu$$

$$\leq C(N^{-r\alpha} + N^{-2} + N^{\alpha-3}), \quad (\text{ for details see [69]}).$$

Hence combining the bounds of R_1 and R_2 completes the proof. □

For smooth solutions case, we choose $r = 1$ that gives uniform mesh grading. Also, since the designed scheme has a CO of $N^{-min\{2-\alpha,r\alpha\}}$ in the temporal direction, choice of $r = (2-\alpha)/\alpha$ would result in the optimal order of convergence.

Theorem 4.3.2. Let $\zeta(x,t)$ be the exact solution to the problem (4.1) satisfying the weak regularity conditions (4.4) and $\{\varpi_i^{j+1},\ 1 \leq i \leq M,\ 0 \leq j \leq n-1\}$ be the numerical solution obtained by the scheme (4.7). Then

$$||\zeta^{n+1} - \varpi^{n+1}||_0 \leq C(N^{-min\{2-\alpha,r\alpha\}} + h^2), \quad \forall \ \ 0 \leq n \leq N-1. \tag{4.21}$$

Proof. Combining Theorem (4.3.1) with Lemma (4.3.3) and equation (4.9) gives the above convergence result. □

4.4 Numerical experiments

In this section some numerical experiments are performed in order to verify the theoretical findings. Also, we investigate the numerical stability of the presented scheme by adding some random perturbations and then simulate their effects on the solution. To calculate the absolute errors in the domain we utilize the following error formulae calculated in $||\cdot||_0$ and $||\cdot||_{H(\chi_{h\tau})}$ norms, respectively, where $||v||_{H(\chi_{h\tau})} = \max\limits_{(x_i,t_n)\in\chi_{h\tau}} |v|$ and $||\cdot||_0$ is the L_2-norm. The errors ($w = \zeta - \varpi$) and order of convergence are listed in the Tables below. The order of convergence in time and space direction are calculated by CO$= \log_{\frac{\tau_1}{\tau_2}} \frac{||w_{h\tau_1}||}{||w_{h\tau_2}||}$ and CO$= \log_{\frac{h_1}{h_2}} \frac{||w_{\tau h_1}||}{||w_{\tau h_2}||}$, respectively.

Example 4.4.1. Let us consider the mathematical model (4.1) with the non-linear source term $f(\zeta) = \zeta - \zeta^3$ and the known linear term

$$G(x,t) = \frac{6t^{4-\alpha}}{\Gamma(5-\alpha)} e^{-bt}\sin(\pi x) + k(t)\Big(m(x,t)\pi^2\sin(\pi x) - t\pi\sin(xt)cos(\pi x) + \sin(\pi x)\big(p(x,t) - 1 + k^2(t)\sin^2(\pi x)\big)\Big),$$

with the coefficients

$$k(t) = \left(1 + \frac{6 - (6 + 6bt + 3b^2t^2 + b^3t^3)}{b^4} e^{-bt}\right),$$

$p(x,t) = 1 - sin(xt)$, $m(x,t) = 2 - \cos(xt)$, $\omega(t) = e^{-bt}$ and $T = 1$. Then the exact solution of the above model is given by $\zeta(x,t) = k(t)\sin(\pi x)$. Since the above problem has a smooth solution, we use the uniform mesh for numerical computations.

Example 4.4.2. Here, in (4.1) taking $f(\zeta) = \zeta^2$ and the known source term

$$G(x,t) = t^{\beta}e^{-bt}\Bigg[\left(\beta t^{-\alpha}\frac{\Gamma(\beta)}{\Gamma(\beta+1-\alpha)} - bt^{1-\alpha}\frac{\Gamma(\beta+1)}{\Gamma(\beta+2-\alpha)}\right)sin(\pi x) + \pi^2\sin(\pi x)m(x,t) - \pi t\sin(xt)\cos(\pi x) + \sin(\pi x)p(x,t) - \sin^2(\pi x)\Bigg],$$

with the coefficients $p(x,t) = 1 - sin(xt)$, $m(x,t) = 2 - \cos(xt)$, $\omega(t) = e^{-5t}$ and T=1. The exact solution is given by $\zeta(x,t) = t^{\beta}\sin(\pi x)e^{-bt}$. Clearly the solution $\zeta(x,t)$ is non-smooth, hence we use the non-uniform grid defined in equation (4.10) for the numerical simulations.

Example 4.4.3. The next example is from [24] having the following data: $g(x,t) = 1$, $h(x,t) = 0$, $\alpha = 0.5$, $G(x,t) = 0$, $w(t) = e^{-5t}$, $T = 1$, and $\zeta_0(x) = \sin(\pi x)$. The non-linear term is taken as $f(\zeta) = \zeta^3$. Here, the exact solution of the problem is unknown and hence we use double computation method on two different grids using the grid defined in (4.10) to find a reference solution. The results are given in Tables 4.6 and 4.7.

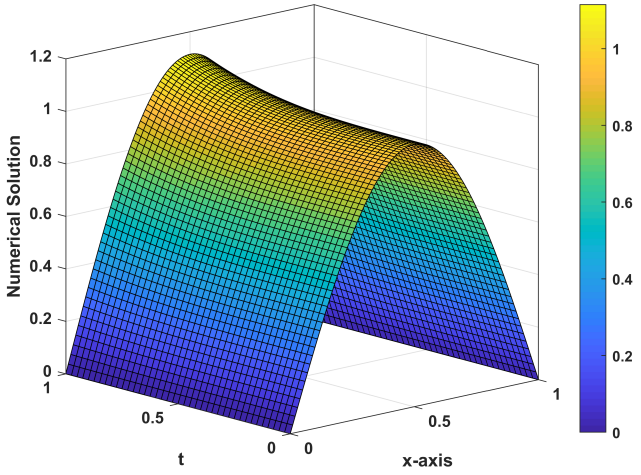

FIGURE 4.1: Numerical Solution of Ex. 4.4.1 for the parameters $\alpha = 0.9$, $N = 40$ and $M = 100$.

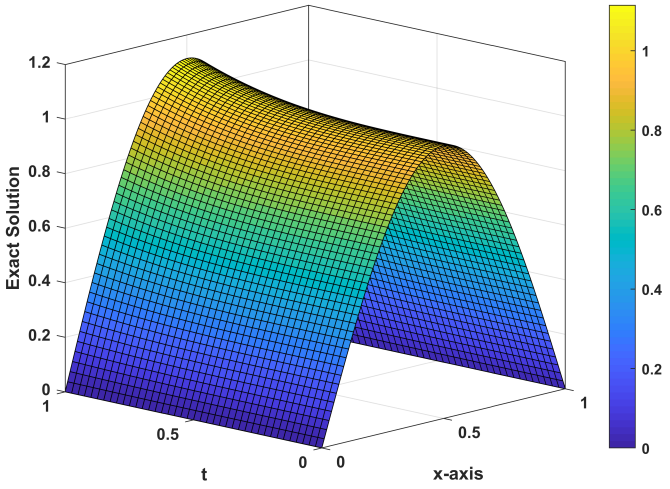

FIGURE 4.2: Exact Solution of Ex. 4.4.1 for the parameters $\alpha = 0.9$, $N = 40$ and $M = 100$.

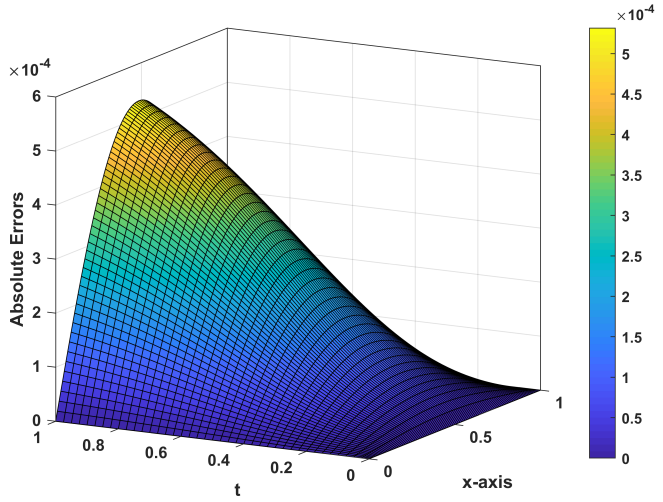

FIGURE 4.3: 3-D error plot for Ex. 4.4.1 for the parameters $\alpha = 0.9$, $N = 40$ and $M = 100$.

TABLE 4.1: Errors and temporal CO for Ex. 4.4.1 with $h = 1/5000$.

b	α	τ	$\|\|w\|\|_{H(\chi_{h\tau})}$	CO	$\max\limits_{0\le n\le N}\|\|w^n\|\|_0$	CO
3	0.2	1/10	1.0224e-04	-	6.8128e-05	-
		1/20	2.6826e-05	1.9303	1.7878e-05	1.9301
		1/40	6.8969e-06	1.9596	4.6031e-06	1.9575
		1/80	1.7878e-06	1.9478	1.1961e-06	1.9443
		1/160	4.7882e-07	1.9006	3.2169e-07	1.8946
2	0.5	1/10	3.3378e-04	-	2.2566e-04	-
		1/20	9.5881e-05	1.7996	6.5205e-05	1.7911
		1/40	2.8049e-05	1.7733	1.9192e-05	1.7644
		1/80	8.4425e-06	1.7322	5.8134e-06	1.7231
		1/160	2.6285e-06	1.6834	1.8213e-06	1.6744
1	0.9	1/10	2.8000e-03	-	1.9000e-03	-
		1/20	1.1000e-03	1.3236	7.7742e-04	1.3119
		1/40	4.6339e-04	1.2682	3.2487e-04	1.2588
		1/80	2.0035e-04	1.2097	1.4110e-04	1.2032
		1/160	8.9311e-05	1.1656	6.3076e-05	1.1615

TABLE 4.2: Errors and spatial CO for Ex. 4.4.1 with $N = 1000$.

α	b	h	$\|\|w\|\|_{H(\chi_{h\tau})}$	CO	$\max_{0\le n\le N}\|\|w^n\|\|_0$	CO
0.2	3	10	6.6000e-03	-	4.7000e-03	-
		20	1.6000e-03	1.9998	1.2000e-03	2.0015
		40	4.1266e-04	1.9980	2.9510e-04	2.0004
		80	1.0316e-04	2.000	7.3773e-05	2.000
0.5	1	10	6.8000e-03	-	4.9000e-03	-
		20	1.7000e-03	1.9928	1.2000e-03	2.0006
		40	4.2649e-04	1.9981	3.0532e-04	1.9990
		80	1.0705e-04	1.9943	7.6592e-05	1.9956
0.9	2	10	6.7000e-03	-	4.8000e-03	-
		20	1.7000e-03	1.9938	1.2000e-03	1.9997
		40	4.2199e-04	1.9923	3.0181e-04	1.9940
		80	1.0744e-04	1.9737	7.6855e-05	1.9734

For Ex. 4.4.1 The results of the numerical experiments performed on the non-linear test problem Ex. 4.4.1 can be described in detail through the following points.

- Table 4.1 shows the L_2 and L_∞ errors and their respective CO obtained in the temporal direction. The spatial discretization parameter has been fixed as $M = 5000$ for computational purpose. Since the exact solution of this test problem has no singularity, we use the uniform temporal mesh. The obtained results clearly state that the developed scheme (4.7) has an accuracy of $2 - \alpha$ in time which confirms the theoretical findings.

- Table 4.2 presents the spatial errors and CO obtained by fixing $N = 1000$ and hence proving a second order of convergence in the spatial direction. Fig 4.1

represents the numerical solution of Ex. 4.4.1 for $\alpha = 0.9$ for $N = 40$ and $M = 100$.

- Figs. 4.2 and 4.3 represent the plots of the exact solution and absolute errors, respectively for $\alpha = 0.9$ for $N = 40$ and $M = 100$. From Figs. 4.1 and 4.2, it can be concluded that the behavior of numerical and the exact solution shows a good agreement.

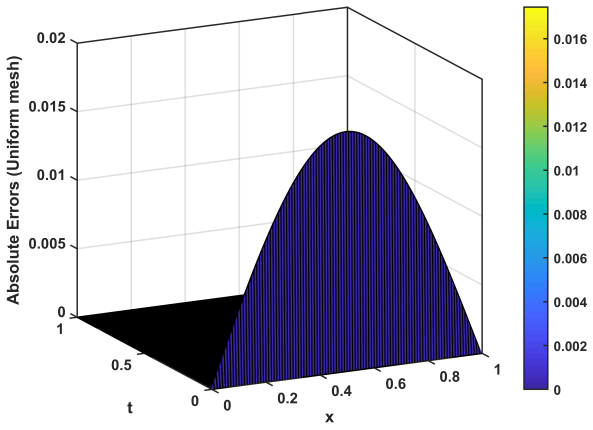

FIGURE 4.4: Absolute Errors of Ex. 4.4.2 on **uniform-mesh** for $\alpha = \beta = 0.3$, $M = N = 100$.
$(\mathbf{r = 1})$

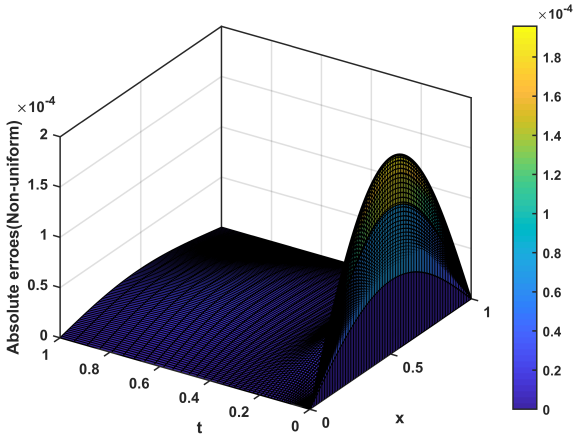

FIGURE 4.5: Error plot on **non-uniform mesh** for $\alpha = \beta = 0.3$, $M = N = 100$.
$(\mathbf{r = (2 - \alpha)/\alpha})$

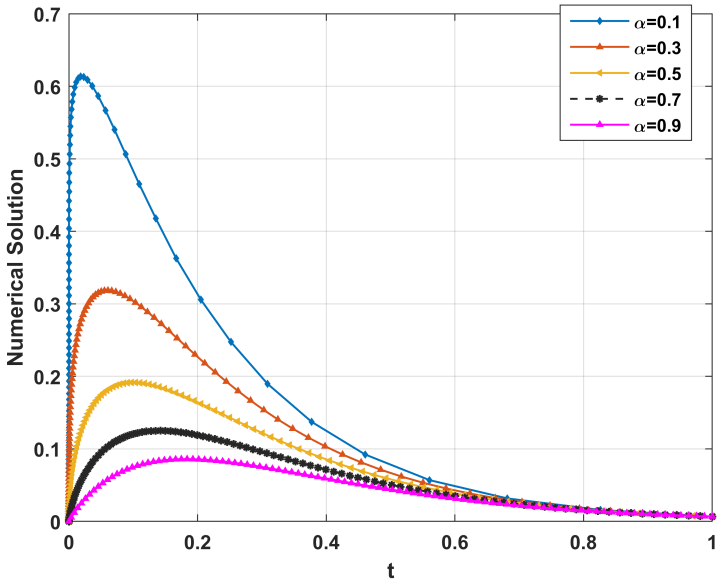

FIGURE 4.6: Numerical Solution of Ex. 4.4.2 for different fractional orders $\alpha = \beta$ at $x = 0.5$.

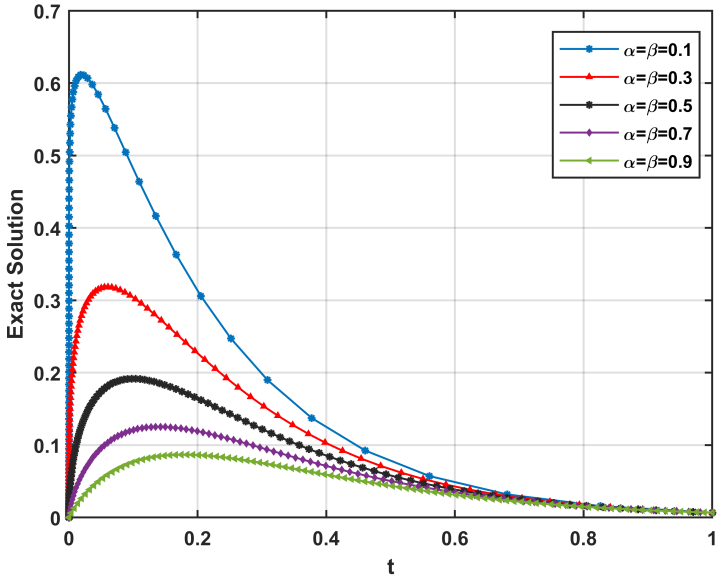

FIGURE 4.7: Exact Solution of Ex. 4.4.2 for different fractional orders $\alpha = \beta$ at $x = 0.5$.

TABLE 4.3: Temporal maximum norm errors and CO for Ex. 4.4.2 with $M = 1000$.

			Uniform grid		**Non-Uniform grid**	
α	β	N	$\|\|w\|\|_{H(\chi_{h\tau})}$	CO	$\|\|w\|\|_{H(\chi_{h\tau})}$	CO
0.3	0.3	40	2.1700e-02	-	7.6853e-04	-
		80	1.8400e-02	0.2387	2.7572e-04	1.4789
		160	1.5700e-02	0.2220	9.3905e-05	1.5539
		320	1.3700e-02	0.2005	3.1228e-05	1.5884
		640	1.2100-02	0.1850	1.0249e-05	1.6073
0.5	0.5	40	1.6300e-02	-	1.3000e-03	-
		80	1.2900e-02	0.3351	5.4143e-04	1.2776
		160	1.0200e-02	0.3344	2.1226e-04	1.3510
		320	8.0000e-03	0.3453	8.0180e-05	1.4045
		640	6.2000e-03	0.3657	2.9606e-05	1.4374
0.9	0.9	40	5.2000e-03	-	3.4000e-03	-
		80	2.8000e-03	0.8924	1.7000e-03	0.9907
		160	1.5000e-03	0.9276	8.4692e-04	1.0169
		320	7.7655e-04	0.9306	4.1436e-04	1.0313
		640	4.0855e-04	0.9266	1.9446e-04	1.0914

For Test Problems 4.4.2 The results of numerical tests performed on problem Ex. 4.4.2 can be described in detail:

- The exact solutions of Ex 4.4.2 is non-smooth and thus we use the non-uniform grid (4.10) with $r = (2 - \alpha)/\alpha$ to obtain the optimal order of convergence.
- Table 4.3 gives a comparison of $||.||_{H(\chi_{h\tau})}$ norm errors and CO obtained on a uniform and non-uniform mesh in time for fixed space parameter $M = 1000$.

The results obtained from the non-uniform grid are far better than the results on uniform mesh due to dense partitioning used near the initial point $t = 0$ to handle the singular behavior of the derivative of the solution at this point.

- Similarly, Table 4.4 presents a comparison of L_2-norm errors and CO obtained on a uniform and non-uniform mesh in time for fixed space parameter $M = 1000$. The non-uniform grid results in $2 - \alpha$ order of convergence whereas uniform grid results only in α order of convergence. Table 4.5 gives second order of convergence in the spatial direction.

- Figs. 4.4 and 4.5 represent the 3-D surface of absolute errors for Ex. 4.4.2 obtained on uniform mesh and non-uniform mesh, respectively. The absolute errors increase as we move closer to the point $t = 0$ and the implementation of the developed scheme on non-uniform mesh yields much lower errors near the point of singularity $t = 0$ as compared to the uniform mesh case.

- Figs. 4.6 and 4.7 are the plots of the numerical solution and the exact solution for Ex. 4.4.2 for several values of α at $x = 0.5$. The graph of the numerical solution agrees well with the graph of the exact solution demonstrating the efficiency of our scheme.

For Test Problems 4.4.3 The results of numerical tests performed on problem Ex. 4.4.3 can be illustrated as follows:

- Since the exact solution of the problem is unknown, hence we use the double computation method on two different grids $\Omega_{h\tau_1}$ and $\Omega_{h\tau_2}$, where $\Omega_{h\tau_1} \subset \Omega_{h\tau_2}$, to find the order of convergence.

- Table 4.6 shows the comparison of maximum norm errors and CO for Ex. 4.4.3, obtained on a uniform and non-uniform mesh in time for a fixed space

parameter $N = 1000$. It can be observed that the results obtained from the non-uniform grid are far better than the results on the uniform mesh.

- Similarly, Table 4.7 presents a comparison of L_2-norm errors and CO for Ex. 4.4.3, obtained on a uniform and non-uniform mesh in time for fixed space parameter $N = 1000$. The non-uniform grid results in $2-\alpha$ order of convergence, verifying the theoretical findings.

4.4.1 Numerical stability

Here we investigate the numerical stability of our presented scheme. For this aim, we add some random perturbed intensity profiles in the given initial data and source terms of the mathematical model (4.1). In all the above test problems the initial data and the source terms without any noisy input are represented as $\zeta_0(x)$, $G(\zeta(x,t))$ and $f(x,t)$, respectively. The perturbed initial data, linear and non-linear source terms are represented by $\zeta_0^\epsilon(x)$, $G^\epsilon(\zeta(x,t))$ and $f^\epsilon(x,t)$, respectively. For obtaining $\zeta_0^\epsilon(x)$, $G^\epsilon(\zeta(x,t))$ and $f^\epsilon(x,t)$ we add a noise term ϵ in $\zeta_0(x)$, $G(\zeta(x,t))$ and $f(x,t)$, respectively. Two parameters m and δ_i are used to control the upper limit of noisy input, where m is a positive real number and δ_i is a uniform random variable that takes values between $[-1,1]$, such that $\zeta_0^\epsilon(x) = \zeta_0(x) + \epsilon\delta_i$, $G^\epsilon(\zeta(x_i,T)) = G(\zeta(x_i,T)) + \epsilon\delta_i$, $f^\epsilon(x_i,T) = f(x_i,T) + \epsilon\delta_i$, for $x_i = ih = 0,1,\ldots M'$, $M'h = L$ and $\underset{0\le x_i\le M'}{max}|\zeta_0^\epsilon(x_i) - \zeta_0(x_i)| < \epsilon$, $\underset{0\le x_i\le M'}{max}|G^\epsilon(\zeta(x_i,T)) - G(\zeta(x_i,T))| < \epsilon$ and $\underset{0\le x_i\le M'}{max}|f^\epsilon(x_i,T) - f(x_i,T)| < \epsilon$.

Table 4

			Uniform grid		**Non-Uniform grid**	
α	β	N	$\max_{0\le n\le N}\|\|w^n\|\|_0$	CO	$\max_{0\le n\le N}\|\|w^n\|\|_0$	CO
0.3	0.3	40	2.17e-02	-	5.4330e-04	-
		80	1.81e-02	0.2632	1.9495e-04	1.4786
		160	1.52e-02	0.2483	6.6399e-05	1.5539
		320	1.29e-02	0.2338	2.2081e-05	1.5884
		640	1.11e-02	0.2246	7.2470e-06	1.6073
0.5	0.5	40	1.53e-02	-	9.2797e-04	-
		80	1.14e-02	0.4188	3.8282e-04	1.2774
		160	8.60e-03	0.4119	1.5008e-04	1.3509
		320	6.50e-03	0.4126	5.6695e-05	1.4045
		640	4.80e-03	0.4203	2.0935e-05	1.4373
0.9	0.9	40	4.8000e-03	-	2.4000e-03	-
		80	2.5000e-03	0.9393	1.2000e-03	0.9906
		160	1.3000e-03	0.9620	5.9873e-04	1.0169
		320	6.4977e-04	0.9719	2.9294e-04	1.0313
		640	3.3108e-04	0.9728	1.3748e-04	1.0914

TABLE 4.4: Temporal L_2-norm errors and CO for Ex. 4.4.2 with $M = 1000$.

Table 5

α	β	h	$\|\|w\|\|_{H(\chi_{h\tau})}$	CO	$\max_{0\le n\le N}\|\|w^n\|\|_0$	CO
0.3	0.3	10	1.6000e-03	-	2.2000e-03	-
		20	3.9074e-04	2.0033	5.5319e-04	2.0034
		40	9.7843e-05	1.9977	1.3852e-04	1.9977
		80	2.4684e-05	1.9869	3.4946e-05	1.9869
0.5	0.5	10	9.2423e-04	-	1.3000e-03	-
		20	2.3016e-04	2.0056	3.2566-04	2.0056
		40	5.7228e-05	2.0079	8.0972e-05	2.0079
		80	1.4037e-05	2.0275	1.9861e-05	2.0275
0.7	0.7	10	5.9963e-04	-	8.4809e-04	-
		20	1.4826e-04	2.0160	2.0968e-04	2.0160
		40	3.5844e-05	2.0483	5.0691e-05	2.0484
		80	8.7870e-06	2.0283	1.2427e-05	2.0283

TABLE 4.5: Spatial errors and CO for Ex. 4.4.2 with $N = 3000$.

Table 6

			Uniform grid		**Non-Uniform grid**	
α	M_1	M_2	$\lvert\bar{\vartheta}_\Omega^{M_1} - \bar{\vartheta}_\Omega^{M_2}\rvert$	CO	$\lvert\bar{\vartheta}_\Omega^{M_1} - \bar{\vartheta}_\Omega^{M_2}\rvert$	CO
0.3	40	80	9.530e-02	-	5.100e-03	-
	80	160	9.160e-02	0.0572	1.900e-03	1.4564
	160	320	8.830e-02	0.0534	6.3187e-04	1.5535
	320	640	8.480e-02	0.0587	2.1018e-04	1.5880
	640	1280	8.0600e-02	0.0722	6.9092e-05	1.6051
0.5	40	80	9.830e-02	-	8.9000e-03	-
	80	160	8.580e-02	0.1962	3.700e-03	1.2760
	160	320	7.110e-02	0.2721	1.400e-03	1.3582
	320	640	5.590e-02	0.3474	5.3083e-04	1.4097
	640	1280	4.200e-02	0.4127	1.9459e-04	1.4478
0.9	40	80	4.690e-02	-	1.5400e-02	-
	80	160	2.580e-02	0.8641	7.600e-03	1.0226
	160	320	1.400e-02	0.8815	3.600e-03	1.0575
	320	640	7.700e-03	0.8694	1.700e-03	1.0878
	640	1280	4.200e-03	0.8520	7.9431e-04	1.1107

TABLE 4.6: Comparison of temporal maximum norm errors and CO for Ex. 4.4.3 on uniform and non-uniform grid with $N = 1000$.

Table 7

			Uniform grid		**Non-Uniform grid**	
α	M_1	M_2	$\max\limits_{0\le n\le M_1} \|\|\bar{\vartheta}^{M_1} - \bar{\vartheta}^{M_2}\|\|_0$	CO	$\max\limits_{0\le n\le M_1} \|\|\bar{\vartheta}^{M_1} - \bar{\vartheta}^{M_2}\|\|_0$	CO
0.3	40	80	6.5500e-02	-	3.6000e-03	-
	80	160	6.2900e-02	0.0576	1.3000e-03	1.4470
	160	320	6.0600e-02	0.0540	4.4820e-04	1.5456
	320	640	5.8200e-02	0.0596	1.4960e-04	1.5831
	640	1280	5.5300e-02	0.0735	4.9298e-05	1.6051
0.5	40	80	6.7800e-02	-	6.2000e-03	-
	80	160	5.9100e-02	0.1988	2.6000e-03	1.2760
	160	320	4.8800e-02	0.2747	1.0000e-03	1.3582
	320	640	3.8300e-02	0.3493	3.7870e-04	1.4097
	640	1280	2.8800e-02	0.4128	1.3950e-04	1.4408
0.9	40	80	2.0500e-02	-	1.2400e-02	-
	80	160	1.0700e-02	0.9431	6.3000e-03	0.9781
	160	320	5.5000e-02	0.9450	3.1000e-03	0.9975
	320	640	2.9000e-03	0.9477	1.6000e-03	0.9600
	640	1280	1.5000e-03	0.9466	7.0885e-04	1.1906

TABLE 4.7: Comparison of temporal L_2-norm errors and CO for Ex. 4.4.3 on uniform and non-uniform grid with $N = 1000$.

For numerical stability analysis, we add three different noisy terms viz. $\epsilon_1 = 0$, $\epsilon_2 = m\%$ of $\mu^{M'}$ and $\epsilon_3 = \sigma^{M'}$ in the above test problems, where $\mu^{M'}$ and $\sigma^{M'}$ represent the mean and standard deviation, respectively.

- The value of $\mu^{M'}$ for linear source term is computed by:

$$\mu^{M'} = \frac{1}{M'+1}\sum_{i=0}^{M'} G(x_i, T),$$

- For the non-linear source term

$$\mu^{M'} = \frac{1}{M'+1}\sum_{i=0}^{M'} f(\zeta(x_i, T)),$$

- The standard deviation (root mean square error) $\sigma^{M'}$ can be computed by

$$\sigma^{M'} = \left(\sum_{i=1}^{M'-1} h\,|\zeta(x_i, T) - \varpi(x_i, T)|^2\right)^{1/2}.$$

For test Ex. 4.1 The following facts about Figs. 4.8, 4.9, 4.10 and 4.11 outline the numerical stability of Example 4.4.1.

- Fig 4.8 represents the numerical solution of Ex. 4.4.1 as U_i^n, $i = 1, 2, \ldots 27$ and $n = 1, 2, 3$ obtained at three distinct time levels T for different values of alpha with noise ϵ_1 added to both initial data and non-linear source term. For labeling purpose, we scale the graph as $U_i^1 = \varpi(x_k, T) + 0.1 \times (i-1)$, $i = 1, 2, \ldots, 9$, $U_i^2 = \varpi(x_k, T) + 0.1 \times (i-10)$, $i = 10, \ldots, 18$ and $U_i^3 = \varpi(x_k, T) + 0.1 \times (i-19)$, $i = 19, \ldots, 27$, $x_k = kh$, $k = 0, 1, 2, \ldots, M'$, $M'h = L$. In the graph, we plotted U^1, $2 \times U^2$ and $3 \times U^3$.

- Fig 4.9 represents the exact solution of Ex. 4.4.1 as Θ_i^m, $i = 1, 2, \ldots 27$ and $n = 1, 2, 3$, obtained at three different time levels T for different alpha. Similar to the numerical solution we scale the graph as $\Theta_i^1 = \zeta(x_k, T) + 0.1 \times (i-1)$, $i = 1, 2, \ldots, 9$, $\Theta_i^2 = \zeta(x_k, T) + 0.1 \times (i-10)$, $i = 10, \ldots, 18$ and $\Theta_i^3 =$

$\zeta(x_k, T) + 0.1 \times (i-19)$, $i = 19, \ldots, 27$, $x_k = kh$, $k = 0, 1, 2, \ldots, M'$, $M'h = L$. In the graph, we plotted Θ^1, $2 \times \Theta^2$ and $3 \times \Theta^3$.

- Fig 4.10 represents the graph of absolute errors between the exact solution and the numerical solution of Ex. 4.4.1 at different time levels T with different α and noise ϵ_1 added to the initial data and non-linear source term. We labeled the errors as E_i^n, $i = 1, 2, \ldots 27$, $n = 1, 2, 3$. The graph is scaled as E^1, $2 \times E^2$ and $3 \times E^3$.

- Two different noises ϵ_1 and ϵ_3 are now added to both the initial data and linear source term for Ex. 4.4.1 for $\alpha = 0.9$, $N = 40$ and $M' = 100$ and the obtained absolute errors are plotted in Fig 4.11. It can be observed from the Figs. 4.8, 4.9, 4.10 and 4.11 that the effect of the addition of different noise terms ϵ_1 and ϵ_3 in initial data and source terms is almost negligible and thus the numerical stability of the designed schemes for the mathematical model (4.1) is confirmed.

For test Examples 4.4.2 The numerical stability and robustness of Ex. 4.4.2 can be described by the following points.

- Fig 4.12 represents the absolute errors graph of Ex. 4.4.2 after the addition of three different noisy inputs viz, ϵ_1, ϵ_2 and ϵ_3 only in the linear source term for $\alpha = 0.3$, $N = 40$ and $M' = 100$.

- Fig 4.13 gives the absolute errors of Ex. 4.4.2 with different noise levels $\epsilon_1 = 0$, $\epsilon_2 = 0.1\%\mu^{100}$ and $\epsilon_3 = \sigma^{100}$ added in both the linear and non-linear source term for $\alpha = 0.3$, $N = 40$ and $M = 100$.

- Figs. 4.12 and 4.13 confirm the numerical stability and efficiency of the designed scheme (4.7) for the problem (4.1) having a non-smooth solution, the derivative of which exhibits a singular behavior at $t = 0$.

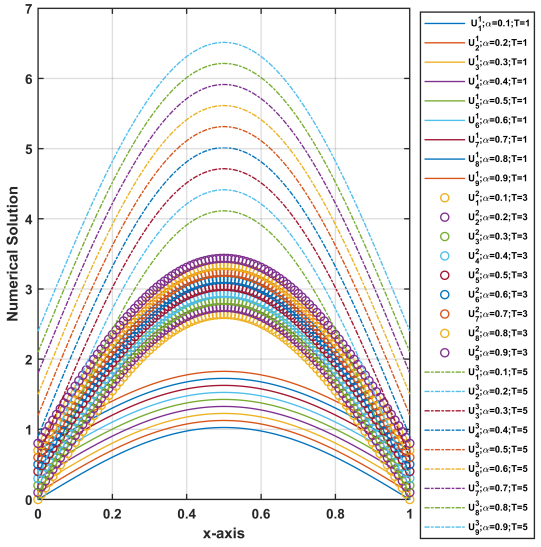

FIGURE 4.8: Numerical Solution of Ex. 4.4.1 with noise ϵ_1 for different α at different time levels T for $N = M' = 100$.

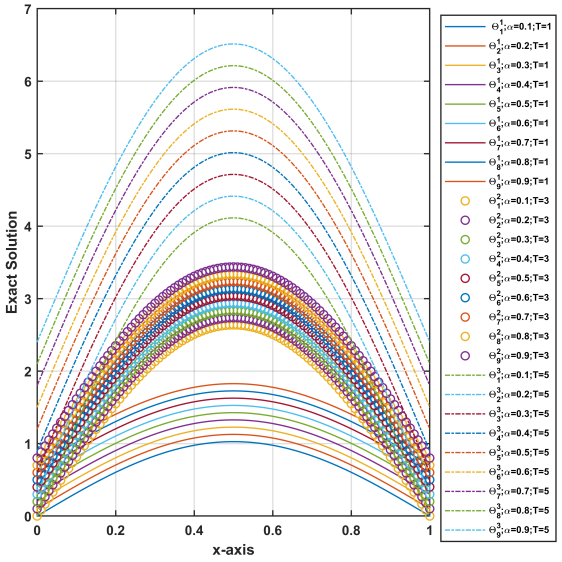

FIGURE 4.9: Exact Solution of Ex. 4.4.1 with noise ϵ_1 for different α at different time levels $T = 1, 3, 5$.

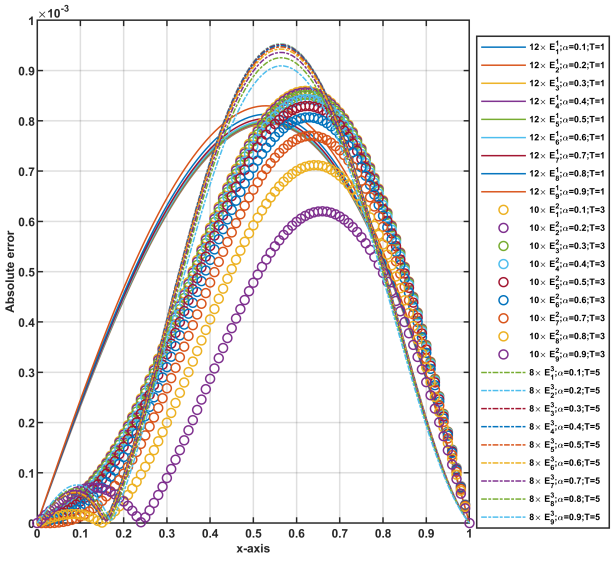

FIGURE 4.10: Absolute Errors for Ex. 4.4.1 with noise ϵ_1 for different α at different time levels T.

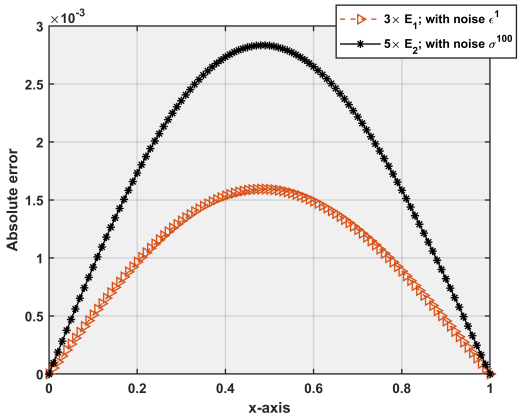

FIGURE 4.11: Absolute errors of Ex. 4.4.1 with different noise levels ϵ_1 and ϵ_3 in both initial data and linear source term for $\alpha = 0.9$ and $N = 40$.

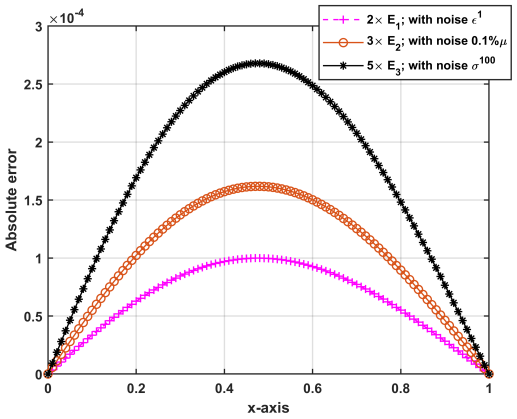

FIGURE 4.12: Absolute Errors of Ex. 4.4.2 with different noise levels in the linear source term for $\alpha = 0.3$ and $N = 40$.

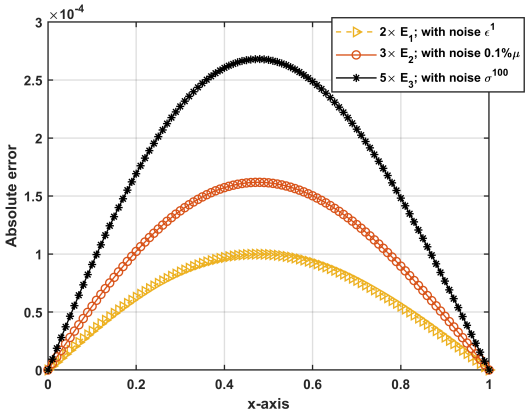

FIGURE 4.13: Absolute Errors of Ex. 4.4.2 with different noise levels ϵ_1, ϵ_2 and ϵ_3 in both linear and non-linear source term for $\alpha = 0.3$ and $N = 40$.

4.5 Conclusion

A robust multistep scheme has been presented for the non-linear (GTFDEs) initial-boundary value problem (4.1). The L1 formula has been utilized on a non-uniform mesh to derive the discrete analog for the generalized Caputo derivative featured by a weight function $\omega(t)$. The non-linear source term has been approximated using Taylor's series. Grid refinement technique has been used near the initial point $t = 0$ to

tackle the singularity of non-smooth solutions. Theorem (4.3.1) and (4.3.2) prove the theoretical stability and convergence of the scheme (4.7) to be $O(N^{-min\{2-\alpha,r\alpha\}}, h^2)$. Three test problems are experimented with, and Tables (4.1)-(4.7) show the numerical efficiency of the developed scheme. A comparison of the results obtained by implementing our proposed scheme on both the uniform grid and non-uniform grid has been provided in Tables 4.3, 4.4, 4.6 and 4.7. The method of using dense partitioning near the point $t = 0$ in the non-uniform discretization yields a CO of $2 - \alpha$ in time whereas uniform mesh results only in α order of convergence. Numerical stability has also been investigated by adding some random noisy disturbances to the initial data, both linear and non-linear source terms. Figs. (4.8, 4.9, 4.10, 4.11, 4.12, 4.13) depict that the effect of noisy inputs is almost negligible on the numerical solution and the approximation errors, thus establishing the robustness of the developed scheme.

✠ This chapter is published in **"Mathematics and Computers in Simulation"**, Vol. 219, 337-354, 2024. **DOI**: https://doi.org/10.1016/j.matcom.2023.12.034

****